Ultrasound Guided Fluorescence Tomography

Baoqiang Li*[a,b], Frédéric Lesage[a,b]

[a]Institute of Biomedical Engineering, École Polytechnique de Montréal, C.P. 6079, succ. Centre-Ville Montreal, QC, Canada H3C 3A7; [b]Montreal Heart Institute, 5000 Bélanger, Montreal, QC, Canada H1T 1C8

ABSTRACT

In this study, a hybrid-model imaging system combining fluorescence and ultrasound (US) was investigated with the motivation of providing structural priors towards improvement of fluorescence reconstruction. A single element transducer was scanned over the sample for anatomy. In the fluorescence part, a laser source was scanned over the sample with the emission received by an EMCCD camera. Synchronization was achieved by a pair of motorized linear stages. Structural information was derived from the US images and a profilometry and used to constrain reconstruction. In the reconstruction, we employed a GPU-based Monte Carlo simulation for forward modeling and a pattern-based method to take advantage of the huge dataset for the inverse problem. Performance of this system was validated with two phantoms with fluorophore inclusions. The results indicated that the fluorophore distribution could be accurately reconstructed. And the system has a potential for the future in-vivo study.

Keywords: Fluorescence, ultrasound, prior information, reconstruction, imaging

1. INTRODUCTION

Hybrid-model imaging methods have been widely studied with the goal of exploiting molecular information. So far, investigations have been conducted to incorporate different anatomical imaging modalities with fluorescence imaging. Several studies combined X-ray CT with fluorescence to better quantify and localize fluorophore distribution. For example, Fang et al combined X-ray imaging with diffuse optical tomography (DOT) for diagnosis of human breast cancer [1]. In a recent study, A. Ale et al combined X-ray CT with FMT and conducted experimental studies with different mice models, which demonstrated that the dual-modality system would be a potent tool for small animal imaging studies [2]. MRI has also been investigated to guide fluorescence functional imaging in both human and small animal scenarios [3–5]. Finally, ultrasound imaging, with the advantages of low cost and non-invasiveness, has been employed as a complement to fluorescence imaging. For example, C. Snyder et al employed US imaging to assess tumor size in mice to provide guidance for fluorescence imaging [6]. Also, Zhu et al used 2D US structural prior for a better fluorescence reconstruction in terms of localization and quantification [7].

In a previous study, we combined 3D US imaging with PMT-based fluorescence tomography to explore both anatomical and functional images, and compared results with previously reported US-Fluorescence systems [8]. Herein, we describe an upgraded system with respect to sampling precision and reconstruction technique. We evaluated this system using two phantoms with different geometries of inserted inclusions in the form of fluorescent tubes. Each tube was filled with Cy5.5 fluorophore at different concentrations. In the fluorescence imaging subsystem, an EMCCD camera was used to image sample from its top side with raster scanned illumination from the opposite side controlled by a pair of motorized linear stages. Acoustic imaging scanning was achieved using the same stages with micrometer step-size to recover accurate structural images. For fluorescence reconstruction, the forward model was simulated by the GPU-based Monte Carlo algorithm [9], and the fluorescence was reconstructed by the Levenberg-Marquardt (LM) minimization method with a regularization term encoding the structural information obtained by US and constraining the inverse problem [10]. Comparing to our previous system, the system described in this paper showed improvements in both optical recording and acoustic sampling. When associated with the GPU-based Monte Carlo reconstruction, this imaging system is expected to result in an improved quantification and localization of fluorophore distribution in-vivo supported by phantom data. Therefore, this multimodal imaging has the promise to contribute in animal study to explore both anatomical and functional information.

*baoqiang.li@polymtl.ca; phone: 514-340-5121 ext. 5022

2. METHOD

2.1 System design

As shown in Fig. 1, a continuous wave (CW) laser beam (658nm, HL6512MG, Thorlabs) was delivered through an optical fiber to illuminate the bottom of sample. Before being coupled into the fiber, the laser beam was filtered by an optical band-pass filter D650/20 (Chroma Technology). On the opposite side, the emitted photons were selected by an optical filter (FF01-716/40, Semrock), then reflected by a mirror and eventually collected by an EMCCD camera (NüvüCamēras). For optical imaging, the region of interest (ROI) was imaged in a raster-scanned fashion controlled by a pair of motorized linear stages (LSM100B, Zaber). For US imaging, a single element transducer was used (10 MHz, Diameter 0.25'', F=10cm, Olympus); and the imaging was conducted in a water media in order to couple ultrasonic pulse-echoes. A home-made electronic board drove the laser diode, pulsed the transducer, sampled ultrasonic signals and communicated with a computer via a USB link. In addition, a projector (PK101, Optoma) projected a white-black pattern on the sample to extract the boundary contour using a FFT profilometry method [11].
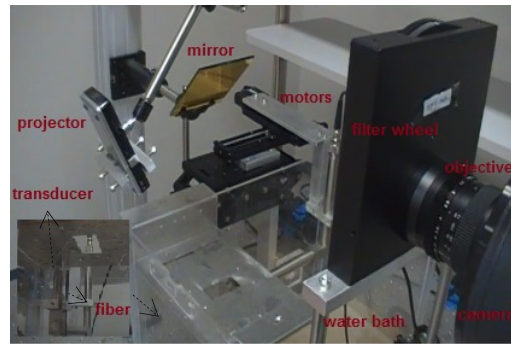

Fig.1. Overview of the system

2.2 Reconstruction

A GPU-based Monte Carlo (MC) algorithm was employed as the solver of forward modeling. The detail of the formularization can be found in Ref. [9]. The reconstruction was performed by the LM method [10] using the update equation (1):

$$\chi_{i+1} = [W^T W + \lambda L^T L] W^T (\Phi_i^{Meas} - \Phi_i^C) + \chi_i \tag{1}$$

where χ is the fluorescence field, herein, the product of extinction coefficient, concentration, and quantum yield of the fluorophore. The term i represents the current iteration number. The matrix L encodes the structural priors; and the regularization term $L^T L$ is incorporated into the update equation to constrain the inverse problem [10]. The terms Φ^{Meas} and Φ^C represent the experimental and simulated measurement, respectively. The weight matrix (or sensitivity matrix) W is simulated by the Monte Carlo method mentioned above, and it can be normalized by a diagonal matrix consisting of the initial value of the fluorescence field [12]. Finally, λ is the regularization parameter which is most commonly defined empirically, or calculated as the square of the ratio of the standard deviation in the measured data to the standard deviation of the unknown [10]; moreover, the value of λ is updated over iterations depending on the change of projection error [13]. The reconstruction converged when the change of the projection error between two iterations was less than 2%. In addition, a maximum of eight iterations was predefined since over eight iterations the error in estimating the unknown tends to increase [10].

Because of the camera-based imaging, the measured dataset is relatively massive. The computation would be considerably time consuming if simulating photon propagations in the reconstruction volume at every pixel was done on the detection side. To avoid high computation as well as extract the efficient information from the measurement, a pattern based reconstruction approach was considered. As explained in Ref. [14], one usually performs a singular-value decomposition (SVD) to simplify the forward model. By this method, the principal components contributed to the reconstruction can be extracted and projected in measurement space so that the most important information can be kept. Therefore, the trimmed dataset results in a more efficient and less massive computation. An example of employing this method was shown in Ref. [15]. Bélanger et al used a pair of digital micro-mirror devices (DMD); one was to generate illumination patterns; another one was to generate detection patterns to convolve with boundary emission. Thus a single

PMT was employed to collect the pattern-convolved emission which resulted in quantitative volumetric reconstruction. Inspired by these works, we incorporated the pattern-based method into the conventional raster-scanned transmission imaging. In the illumination side, the laser source was scanned over the ROI point by point. However, in the detection side, each image was convolved with a detection pattern. There, a detected image having many pixels could be reduced to a single data of measurement. In fact, for each image, several patterns consisting of sinusoidal waves of different frequencies were used. Typically, patterns of low spatial frequencies were preferably employed because the most important signal of diffuse fluorescence imaging was at low frequencies.

3. EXPERIMENTS

3.1 Phantoms

We characterized the system and evaluated the reconstruction using two homogeneous phantoms. (1) The first one was a semi-cylinder geometry of ~18 mm diameter, and with optical properties of μ_s'=1 mm^{-1} and μ_a=0.01 mm^{-1}; (2) the second one was a semi-cylinder geometry of ~15 mm diameter with optical properties of μ_s'=1 mm^{-1} and μ_a=0.01 mm^{-1}. As shown in Fig. 2, in the first phantom, one hole was made so that a cylindrical fluorescent tube having varying diameters (from ~2 mm to ~4 mm) could be inserted. In the second phantom, a node shaped tube of inner diameter ~1mm was included during molding.
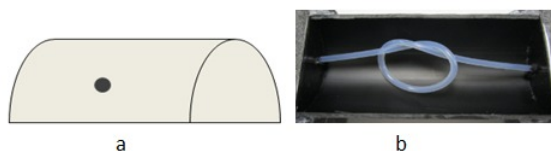

Fig. 2. a. The schematic of the first phantom; b. the inclusion tube in the second phantom.

3.2 Experiment

In experiments, a concentration of 250nM Cy5.5 was injected into the tubes of the two phantoms, respectively. As the Fig. 3 shows, different ROIs (in color) were imaged for each phantom. For every phantom, the laser source was scanned with 2 mm steps. The scan steps were ~100 μm for acoustic recording for every case. In Fig. 3-a, the fluorescence image is overlaid on the picture of the phantom. The intensity of the fluorescence signal varied according to the change of the tube dimension along its length. In Fig. 3-b, the patterned image from the projector for this phantom is shown. From the phase shift of the white-black lines, the surface contour was extracted using a FFT profilometry algorithm [11]. The obtained contour of the first phantom is shown in Fig. 3-d. In Fig. 3-c, one slice of US image is presented. The slice is along the Y axis and across the middle position of the X axis according to the ROI shown in color in Fig. 3-a. Results for the second phantom were similar. As shown in Fig. 3-e, the fluorescence signal overlaid on the phantom picture was presented. Also, in Fig. 3-f, the patterned image was presented. However, because both of these two phantoms have similar geometry, only the contour of the first phantom was presented. Finally, three slices of US image were shown in Fig. 3-g/-j/-i. The slices are along the Y axis and across three different positions of the X axis according to the ROI shown in color in Fig. 3-e. As shown, the US images of the second phantom suffered from secondary echoes. This could be solved by adjusting the distance between the transducer and the sample.
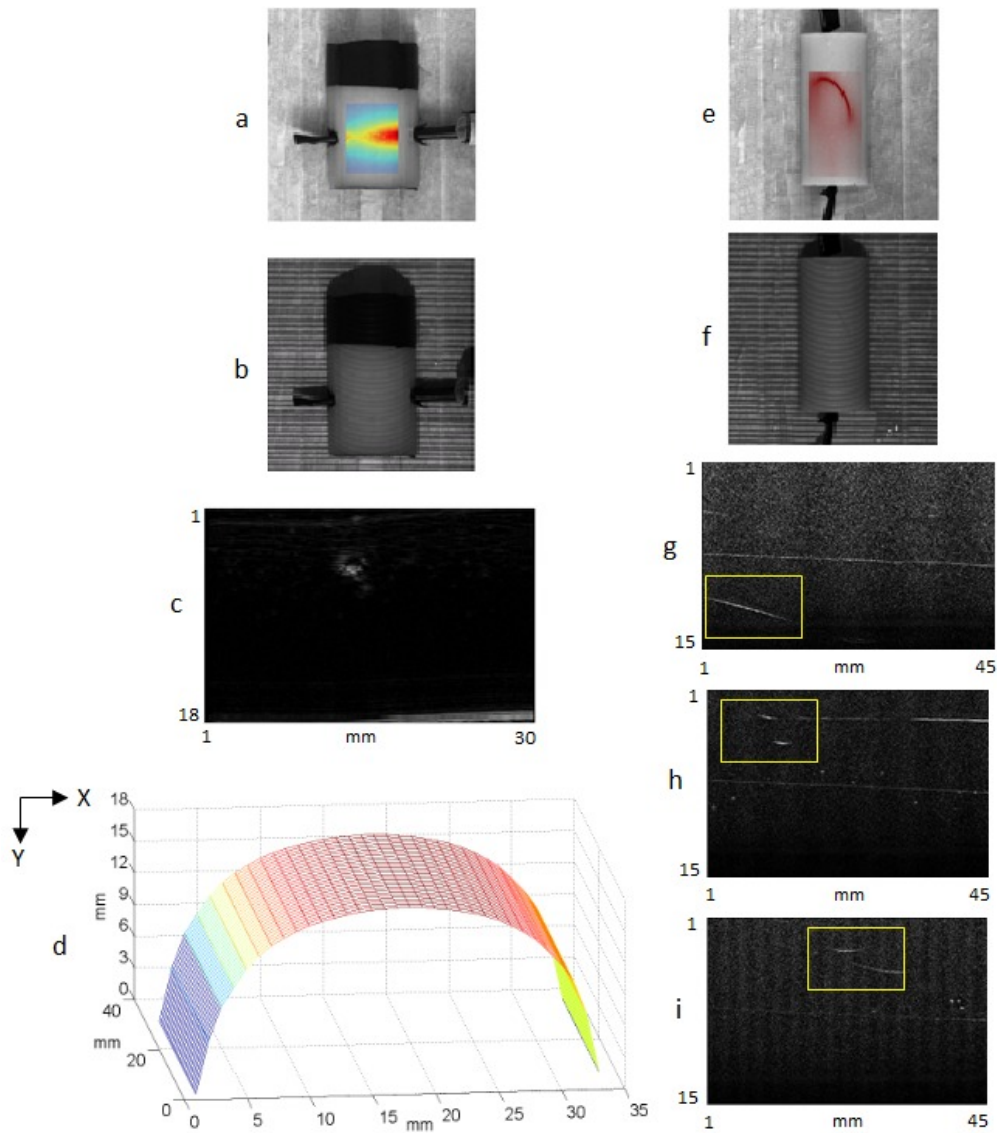
Fig. 3. The 1st phantom: a. fluorescence signal overlaid on the picture of the phantom; b. image with white-black strips pattern; c. a slice of US image; d. the surface contour. The 2nd phantom: e. fluorescence signal overlaid on the picture of the phantom; f. image with white-black strips pattern; g-i. three slices of US image as marked by the square in yellow color.

The reconstruction was performed using the method described in the section 2.2. For the forward problem of each phantom, a rectangular parallelepiped volume was created; and by incorporating the information of the contour, air was put in the simulation to be separated from the region of phantom. Herein, as mentioned in the last subsection, a set of homogenous optical properties was assumed in each phantom. The fluorescent tube was not distinguished by different optical properties to simulate an in-vivo case, in which the optical properties of lesion would not be often known. Moreover, in order to provide structural priors of the inclusions for the reconstruction, the US images had to be segmented. For the first phantom, the region of the fluorescent tube was segmented using a threshold. However, for the second phantom, of which the structure of inclusion is much more complicated, the fluorescent tube was segmented manually. Thus, the US structural information was used as a soft-prior to constrain the reconstruction [10]. Again, to simulate an in-vivo case, same homogenous initial values were used in both phantoms. As mentioned above, the reconstructed fluorescence field is the product of fluorophore concentration, quantum yield, and extinction coefficient. In every reconstruction, we used quantum yield of 0.23 and extinction coefficient of 2.5×10^{-5} mm^{-1}nM^{-1}, which can be

found in the product datasheet; and we initiated the iteration from the concentration of 170 nM. Assumingly, the quantum yield and the extinction coefficient were constant, thus the value of concentration was updated by reconstruction. For the regularization parameter, we empirically chose 6 as an initial value for all the cases. However, the regularization strategy requires the regularization parameter to be adjusted upon the standard deviation of the measurement. Here we made a hypothesis that the segmented region from the US images would not be the only region to fluoresce, which would be common in animal experiments. Therefore, we kept the regularization parameter constant as well as using the same initial value throughout all the reconstructions in order to compare the results in a consistent way. The reconstructed images are presented in Fig. 4. As shown in Fig. 4-a, the reconstructed fluorophore concentration was shown. And the changing diameter of the fluorescent tube along its length could be seen. In the Fig. 4-b, the concentration was reconstructed according to the segmented fluorescent region. However, the concentration of fluorophore was overestimated in some voxels. The cause will be discussed in the next subsection.
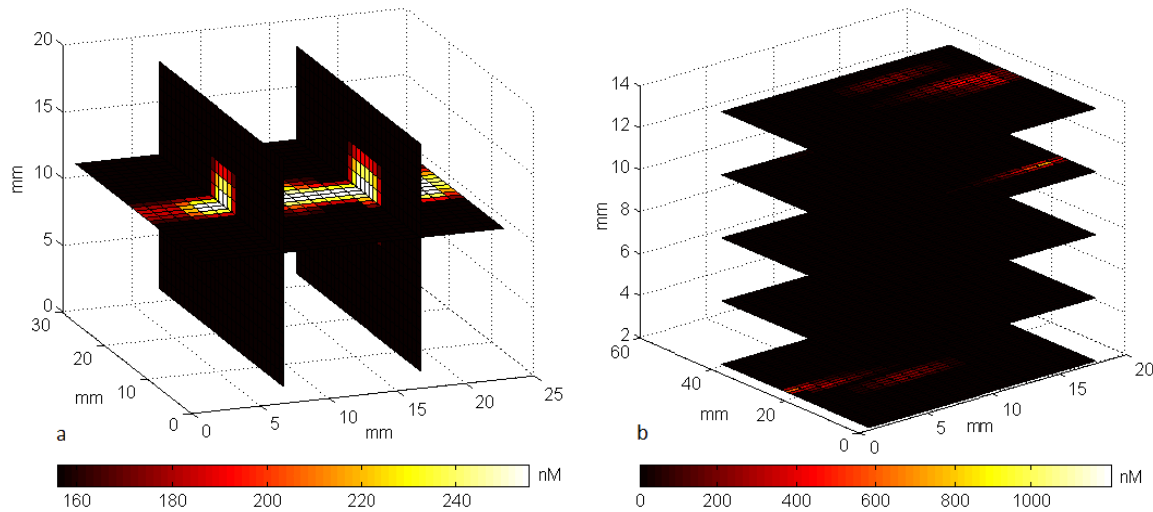

Fig. 4. a. Slices of the fluorescence reconstruction of the first phantom; b. slices of the fluorescence reconstruction of the second phantom.

3.3 Analysis of the reconstruction

In this last subsection, two phantom experiments were done. Inclusions with Cy5.5 fluorophore at 250nM was injected into the tubes inside the two phantoms, respectively. With the spatial priors derived from the profilometer and the US imaging, the fluorophore distribution was reconstructed. After, another group of phantom experiments using the same phantoms but with the Cy5.5 fluorophore concentration at 500nM was further conducted. Without presenting the reconstructed images, the quantification was compared for all the four cases in the Fig. 5. In this figure, the bars present the average concentration of the segmented fluorescent region for each case. Above each bar, the reconstruction precision in percentage is denoted. From the figure, one could see that the reconstruction precision is up to 91% in the first case (Phantom-1, 250nM). But it was overestimated for the second phantom (Phantom-2, 250nM). For the second phantom, the measured fluorescence had lower contrast because diffusion potentially played a role in decreasing the value due to poor spatial resolution. And as mentioned above, we empirically chose 6 as the value of regularization parameter which was tested to be good for the first case; and then kept this constant value for all the cases. So, the reconstruction precision was 91% for the first case but deteriorated for the other experiments. In addition, although the reconstruction precision was 80% in the second phantom (Phantom-2, 250nM), some voxels were highly overestimated as shown in Fig. 4-b. The same problem was observed when fluorophore of 500nM was used in this phantom (Phantom-2, 500nM).

Further, the contrast to noise ratio (CNR) was compared across the reconctructions. The CNR is defined as the ratio of the reconstruction contrast value to the noise, where the contrast is calculated as the absolute difference of the reconstructed fluorophore concentration between the segmented fluorophore region and the background region; the noise is the standard deviation of the background.The CNR was 8.38, 5.18, 7.28 and 7.29 for the cases shown in Fig. 5 in the order from left to right. The first case has the best CNR value which is qualitatively in agreement with the reconstruction

results. However, the CNRs of the reconstruction of the second phantom were lower than those of the first phantom at both concentrations. That was because lower camera gain was used for the second phantom because of its smaller dimension, which implyed a lower signal to noise ratio (SNR) of the measurement.
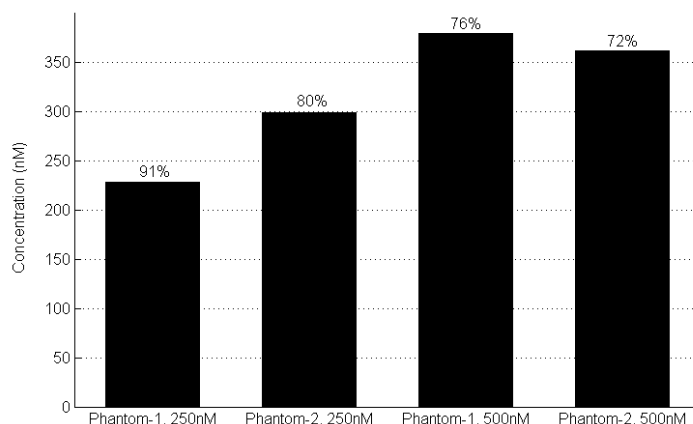

Fig. 5. Quantification of the reconstructions.

4. DISCUSSION

In this paper, we presented the design of a dual-modality imaging system combining fluorescence and ultrasound. Comparing to our first version, this system was upgrated with respect to optical sampling and acoustic recording. Benefiting from the US image and the boundary contour, one could extract the structural prior information for the reconstruction, which has been already reported by several studies being beneficial to the reconstruction. Associated with the imaging strategy, we described the reconstruction technique to take advantage of the huge dataset. Using the GPU-based Monte Carlo method, we simulated the photon propagation for the forward model. With this technique, we managed to compute a sensitivity matrix encoding the relationship between a point-based illumination and a pattern-based detection. For the inverse problem and image reconstruction, we convoluved each pattern image with every detected image as one measurement. To be specific, a total of 32 sinusoidal patterns of different spatial frequencies images were chosen. The spatial frequencies were from $\pi/4$ to 4π, which was expected to extract the low-frequency components of the measurement. Overall, with this reconstruction mechanism, we reduced the size of measurement but kept the more important part of it for the reconstruction. Finally, to evaluate the reconstrutions from different experiments in a consistent way, we used a constant set of reconstruction parameters. Consequently, the reconstruction precision was 72% in the worst case and 91% in the best. And in all cases, the CNR was above 5.

Improvement could be achieved upon the following modifications. First, functional priors might be included in the forward modelling in order to get a more realistic sensitivity matrix. Moreover, the pattern images could be optimised so that the maximal information will be extracted from the detected images without increasing the number of patterns.

5. CONCLUSION

In this paper, a dual-modality imaging system was introduced. While the study has been limited to phantoms, it indicates potential for application in animals. The extension of this study will be molecular imaging with cancerous mice.

REFERENCES

[1] Qianqian Fang, S. A. Carp, J. Selb, G. Boverman, Quan Zhang, D. B. Kopans, R. H. Moore, E. L. Miller, D. H. Brooks, and D. A. Boas, "Combined Optical Imaging and Mammography of the Healthy Breast: Optical Contrast Derived From Breast Structure and Compression," *Medical Imaging, IEEE Transactions on*, vol. 28, no. 1, pp. 30–42, 2009.

[2] A. Ale, V. Ermolayev, E. Herzog, C. Cohrs, M. H. de Angelis, and V. Ntziachristos, "FMT-XCT: in vivo animal studies with hybrid fluorescence molecular tomography-X-ray computed tomography," *Nature Methods*, vol. 9, no. 6, pp. 615–620, 2012.

[3] S. C. Davis, B. W. Pogue, R. Springett, C. Leussler, P. Mazurkewitz, S. B. Tuttle, S. L. Gibbs-Strauss, S. S. Jiang, H. Dehghani, and K. D. Paulsen, "Magnetic resonance–coupled fluorescence tomography scanner for molecular imaging of tissue," *Rev Sci Instrum*, vol. 79, no. 6, May 2008.

[4] B. A. Brooksby, H. Dehghani, B. W. Pogue, and K. D. Paulsen, "Near-infrared (NIR) tomography breast image reconstruction with a priori structural information from MRI: algorithm development for reconstructing heterogeneities," *Selected Topics in Quantum Electronics, IEEE Journal of*, vol. 9, no. 2, pp. 199–209, 2003.

[5] Y. Lin, M. T. Ghijsen, H. Gao, N. Liu, O. Nalcioglu, and G. Gulsen, "A photo-multiplier tube-based hybrid MRI and frequency domain fluorescence tomography system for small animal imaging," *Physics in Medicine and Biology*, vol. 56, no. 15, pp. 4731–4747, Jul. 2011.

[6] C. Snyder, S. Kaushal, Y. Kono, H. Tran Cao, R. Hoffman, and M. Bouvet, "Complementarity of ultrasound and fluorescence imaging in an orthotopic mouse model of pancreatic cancer," *BMC Cancer*, vol. 9, no. 1, pp. 106, 2009.

[7] Q. Zhu, M. Huang, N. Chen, K. Zarfos, B. Jagjivan, M. Kane, P. Hedge, and H. S. Kurtzman, "Ultrasound-Guided Optical Tomographic Imaging of Malignant and Benign Breast Lesions: Initial Clinical Results of 19 Cases," *Neoplasia*, vol. 5, no. 5, pp. 379–388, Sep. 2003.

[8] B. Li, M. Abran, C. Matteau-Pelletier, L. Rouleau, T. Lam, R. Sharma, E. Rhéaume, A. Kakkar, J.-C. Tardif, and F. Lesage, "Low-cost three-dimensional imaging system combining fluorescence and ultrasound," *Journal of Biomedical Optics*, vol. 16, no. 12, pp. 126010, Dec. 2011.

[9] Q. Fang and D. A. Boas, "Monte Carlo simulation of photon migration in 3D turbid media accelerated by graphics processing units," *Opt. Express*, vol. 17, no. 22, pp. 20178–20190, Oct. 2009.

[10] P. K. Yalavarthy, B. W. Pogue, H. Dehghani, and K. D. Paulsen, "Weight-matrix structured regularization provides optimal generalized least-squares estimate in diffuse optical tomography," *Med. Phys.*, vol. 34, no. 6, pp. 2085, 2007.

[11] M. Takeda and K. Mutoh, "Fourier transform profilometry for the automatic measurement of 3-D object shapes," *Appl. Opt.*, vol. 22, no. 24, pp. 3977–3982, Dec. 1983.

[12] H. Dehghani, M. E. Eames, P. K. Yalavarthy, S. C. Davis, S. Srinivasan, C. M. Carpenter, B. W. Pogue, and K. D. Paulsen, "Near infrared optical tomography using NIRFAST: Algorithm for numerical model and image reconstruction," *Communications in Numerical Methods in Engineering*, vol. 25, no. 6, pp. 711–732, 2009.

[13] S. Srinivasan, B. W. Pogue, H. Dehghani, S. Jiang, X. Song, and K. D. Paulsen, "Improved quantification of small objects in near-infrared diffuse optical tomography," *J Biomed Opt*, vol. 9, no. 6, pp. 1161–1171, Nov. 2004.

[14] V. A. Markel, V. Mital, and J. C. Schotland, "Inverse problem in optical diffusion tomography. III. Inversion formulas and singular-value decomposition," *J. Opt. Soc. Am. A*, vol. 20, no. 5, pp. 890–902, Apr. 2003.

[15] S. Bélanger, M. Abran, X. Intes, C. Casanova, and F. Lesage, "Real-time diffuse optical tomography based on structured illumination," *J Biomed Opt*, vol. 15, no. 1, pp. 016006, Jan. 2010.